The Lunar Flashlight CubeSat instrument: A compact SWIR laser reflectometer to quantify and map water ice on the surface of the Moon

Udo Wehmeier[a], Quentin Vinckier[a], R. Glenn Sellar[a] , Christopher G. Paine[a], Paul O. Hayne[b], Mahmood Bagheri[a], Mina Rais-Zadeh[a], Siamak Forouhar[a], Jessica Loveland[a], Jacob Shelton[a]
Jet Propulsion Laboratory, California Institute of Technology, 4800 Oak Grove Dr, Pasadena, CA, USA 91109; [b]University of Colorado, 391 UCB, Boulder, CO, USA 80309

ABSTRACT

The Lunar Flashlight (LF) mission will send a CubeSat to lunar orbit via NASA's Space Launch System (SLS) test flight. The LF spacecraft will carry a novel instrument to quantify and map water ice harbored in the permanently shadowed craters of the lunar South Pole. The LF instrument, an active multi-band reflectometer which employs four high power diode lasers in the 1-2 µm infrared band, will measure the reflectance of the lunar surface near water ice absorption peaks. We present the detailed instrument design and system engineering required to deploy this instrument within very demanding CubeSat resource allocations.

Keywords: CubeSat, Lunar Flashlight, reflectometer, laser, radiometry, remote sensing.

1. INTRODUCTION

Mapping and quantifying lunar water ice addresses one of NASA's Strategic Knowledge Gaps to understand the lunar resource potential for future human exploration of the Moon. Lunar Flashlight is an innovative NASA CubeSat mission dedicated to mapping water ice in the permanently shadowed and occasionally sunlit regions in the vicinity of the lunar South Pole. Lunar Flashlight (LF) will acquire these measurements from lunar orbit using a multi-band laser reflectometer composed of an optical receiver aligned with four lasers emitting different wavelengths in the shortwave infrared spectral region between 1 µm and 2 µm. Considering the constraints of a CubeSat spacecraft bus, the design of this instrument has prompted many trades and novel solutions to satisfy mass, volume, power, and thermal requirements. We present an overview of the system design, details of the subsystem implementations, and the system engineering used in developing this instrument. It is expected that the LF instrument will demonstrate several firsts, including being one of the first instruments onboard a CubeSat performing science measurements beyond low Earth orbit and the first planetary mission to use multi-band active reflectometry from orbit.

2. PROGRAM OBJECTIVES AND REQUIREMENTS

2.1 Mission goals and Strategic Knowledge Gaps

For nearly a century, predictions have been made for the existence of stable ice deposits in the permanently shadowed craters of the Moon[1,2]. In such craters located near the lunar poles, temperatures are low enough (<110 K) to trap volatiles, such as H_2O, NH_3, CO_2, or H_2S, in their solid state for up to billions of years[3–5]. Mapping and quantifying lunar volatiles, in particular water, associated with these cold traps addresses one of NASA's Strategic Knowledge Gaps (SKG) to understand the lunar resource potential for future human and robotic exploration of the moon[6]. In addition, this data is also crucial to addressing outstanding questions in planetary science, such as testing hypotheses regarding the delivery and retention of water and other volatiles in the inner Solar System.

Over the past two decades, several orbital and flyby missions have revealed strong indications of the presence of lunar water ice using a wide range of techniques[7–27]. Due to limitations of the measurements thus far acquired, interpretations are varied and no consensus has yet been achieved as to the form, quantity, or distribution of lunar H_2O at concentrations sufficient for in-situ resource utilization (ISRU)[3,5,13,25].

The Lunar Flashlight (LF) spacecraft is a '6U' CubeSat designed to orbit the Moon to detect, quantify, and map lunar H_2O ice in the permanently-shadowed regions and occasionally-sunlit regions of the Moon for potential ISRU. LF's instrument, a multi-band reflectometer, will measure zero-phase-angle surface reflectance at four different wavelength bands between 1 µm and 2 µm in the shortwave infrared (SWIR) wavelength region[28,29]. One of these bands, the 1.064 µm band, has been chosen to enable comparison with data acquired by the Lunar Orbiter Laser Altimeter (LOLA)[25–28, 30–32]. LF will be one of the first CubeSats performing science measurements beyond low Earth orbit (two other CubeSat missions have been selected to make complementary lunar volatile measurements[33,34]) and the first planetary mission to use multi-band active reflectometry from orbit.

2.2 Launch on SLS as EM-1 secondary payload

The test flight EM-1 of the SLS launch vehicle, scheduled to launch no sooner than December 2019, will carry thirteen low cost CubeSats to cislunar orbit as a secondary payload. NASA's Advanced Exploration Systems (AES) program selected three of these CubeSat missions. The Lunar Flashlight (LF) mission was selected as one of these missions, specifically to address the SKG associated with lunar volatiles.

2.3 CubeSat form factor

Lunar Flashlight will inherit the compact form factor of the CubeSat "CSD" standard, being a 6U bus measuring 12x24x36 cm. The CubeSats to be launched by EM-1 will use the Tyvak CubeSat dispenser to provide low cost and reliable deployment. Hence, each CubeSat must comply with rigorous safety and environmental requirements. The CubeSat form factor also limits spacecraft mass to less than 14 kg, and the LF power budget will be less than 60 W on orbit average.

As is common with CubeSats, Lunar Flashlight is a single string design with limited fault redundancy and may carry COTS components which have been screened for use in space application. The Lunar Flashlight bus will also feature a novel propulsion system by VACCO using "green propellant" and novel miniaturized flight electronics (Phoenix CDH board) and Radio (IRIS) for deep space operation. Some of these elements have been proven on the recently launched MARCO CubeSats to Mars. After deployment from the dispenser, LF will deploy four solar panels in the configuration shown in Figure 2-1.

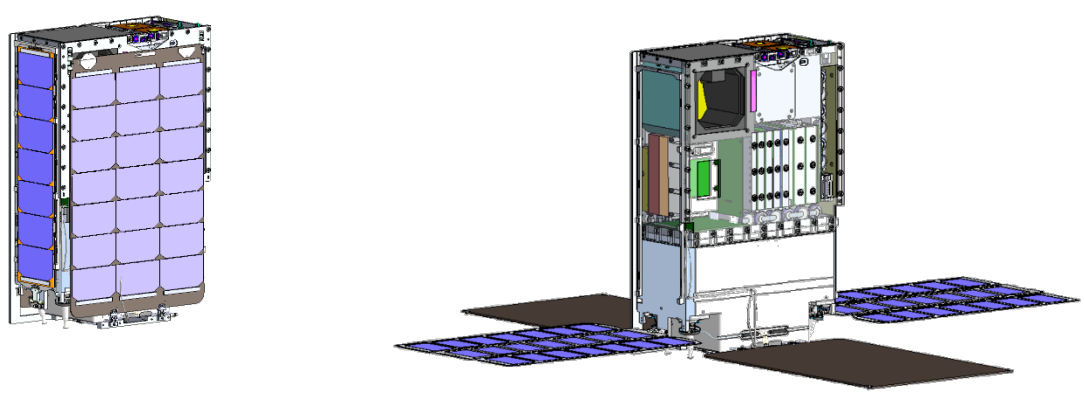

Figure 2-1 Lunar Flashlight CubeSat in storage (left) and deployed (right)

2.4 Science goals

The goal of the LF mission is to identify locations where water ice is present on the lunar surface with a mapping resolution of 1-2 km (10 km for the minimum success criteria). To achieve this goal, the LF instrument employs an optical receiver aligned with four high-power diode lasers, each emitting in a different wavelength band in the 1-2 µm SWIR spectral region. The instrument will target regions near the South Pole called "permanently shadowed regions" (PSRs), which do not receive sunlight over billions of years, and which may therefore be expected to harbor water ice. The science goal of the mission is to map these features in comparison to nearby sunlit surfaces, and measure the water ice content of the lunar regolith based on a "percent weight" metric where water concentrations are expected between 0% and 5%.

2.5 Mission design

During the planned two-month primary mission, LF will be placed in a near-rectilinear orbit about the moon. During 10 of these orbits, LF will execute science encounters targeting PSRs from altitudes of 12.6-52.4 km within 10° latitude of the lunar South Pole. While not permitting a complete survey of the Lunar South Pole, this mission profile will allow optimum targeting of PSRs based on resources available to the spacecraft. The map of PSRs and proposed orbit are shown in Figure 2-2.

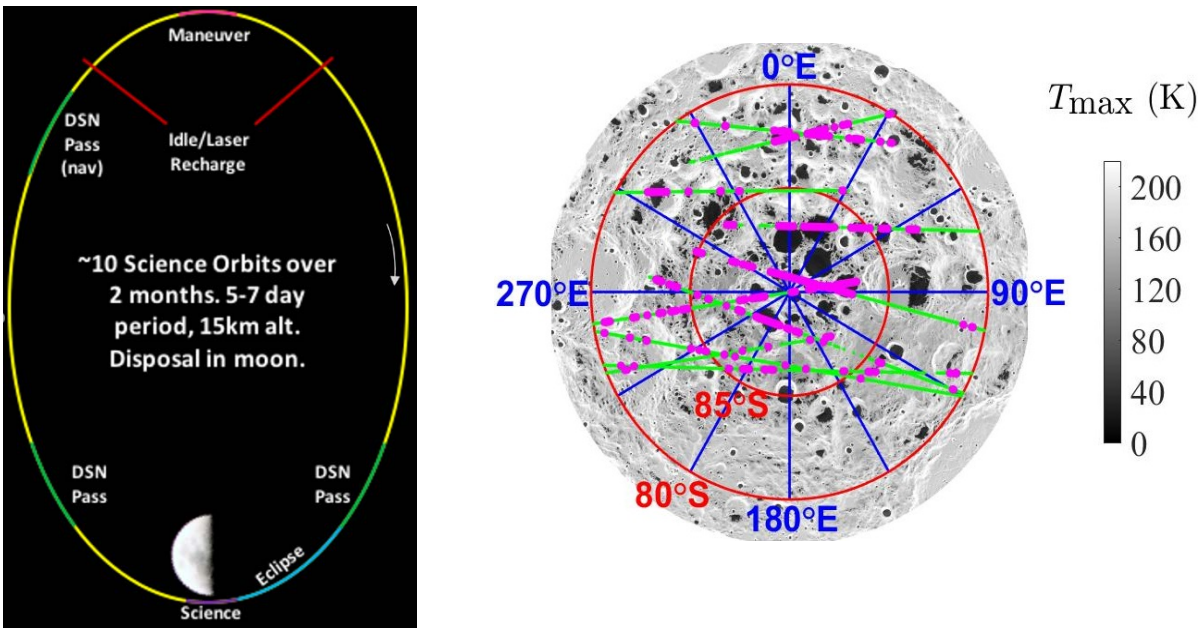

Figure 2-2 Lunar Orbit (left) and LF spacecraft Science data paths on the lunar South Pole (right). The gray scale shows the maximum temperature; the green and pink segments are the Science paths with the pink dots indicating the PSRs.

2.6 Instrument Technology

The Lunar Flashlight instrument is novel in its design and implementation in many ways to meet the size, mass, power, and thermal constraints of the CubeSat form factor. To enable a compact active reflectometer, LF employs a compact high power diode laser which emits an IR beam at optical power up to 72W. Novel technology is also employed to manage the thermal load of the laser, as this is absorbed during the short time of fire by a phase change material (PCM) that later transfers the heat more slowly to the spacecraft bus from which it is rejected as thermal radiation. The laser electrical power system (L_EPS) was developed to take advantage of compact lithium ion (Li-ion) battery technology to provide the energy needed to drive the laser. The L_EPS was designed to meet the challenges of dissipating thermal load of the power electronics in a small volume. In addition, instrument electronics were developed to occupy a compact package but with the ability to be tuned to deliver the high SNR required of this instrument.

The Lunar Flashlight mission was originally conceived to use solar sail propulsion as well as to use the same solar sail as an illumination method. Through optimization of spacecraft and mission resources, this approach was refined to accommodate a custom and unique “green propellant” propulsion system by VACCO Industries, Inc., and the laser illuminator by Coherent DILAS, Inc., as described. These novel developments will be demonstrated on orbit to improve their technology readiness level (TRL) during this mission.

3. LUNAR FLASHLIGHT INSTRUMENT OVERVIEW

3.1 Instrument Layout

The Lunar Flashlight CubeSat carries a single payload. The LF instrument occupies 2U in a 6U spacecraft and is designed to be extremely compact and of low mass. The instrument assembly is designed to be modular to facilitate integration and test independent of the CubeSat bus, unlike typical CubeSat designs which result in tightly coupled payload and bus structures. The instrument is supported by a "sideplate" which supports the optical receiver and the laser emitter in a very precise and stiff mechanical structure, as shown in Figure 3-1. The receiver comprises a 70 mm off-axis parabolic mirror (OAP) and a baffle assembly to shield the InGaAs detector from stray light. The detector is cooled by an aluminum radiator which is mounted on the receiver body and radiates to deep space. The Laser is mounted on the PCM box for thermal dissipation, and L_EPS are also mounted to this structure. The instrument main electronics, the Digital (DPLE) and Analog (APLE) PayLoad Electronics board, are mounted to the CubeSat frame as shown in Figure 3-1. The three Li-ion batteries are mounted to the midplate to provide power for the Laser.

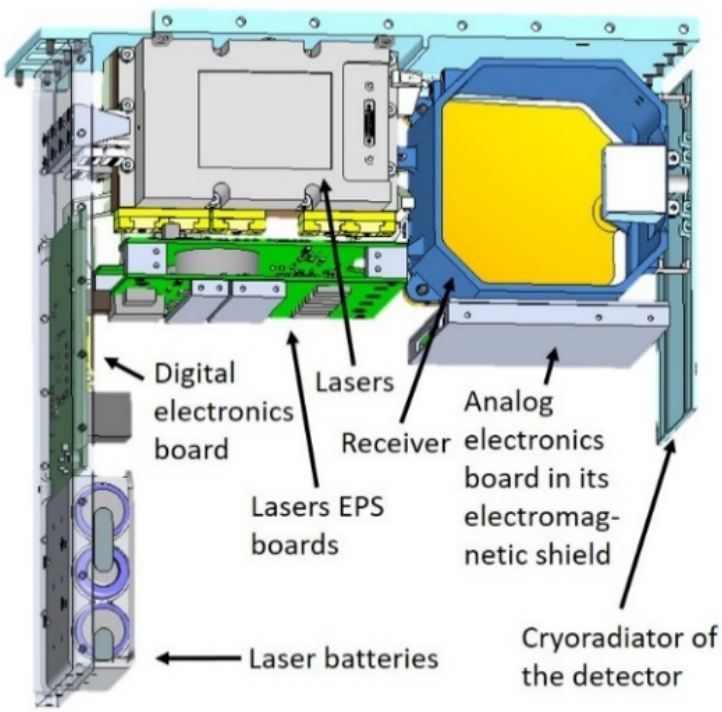

Figure 3-1 Lunar Flashlight 2U multi-band SWIR reflectometer.

3.2 Instrument principle of operation

The LF instrument requires the precise co-alignment of the four diode lasers and optimization of the field of view (FOV) of the receiver to minimize errors in the measured reflectances.

The diode lasers, supplied with 45 A current from L_EPS board and laser batteries, emit optical powers from 15 W to 73 W (depending on wavelength) in the 1-2 µm SWIR spectral region. The laser beam profile requirement is that 99.6% of the emitted energy is encircled within a full-angle of 17 mrad. The receiver is based on an off-aperture uncoated aluminum paraboloidal mirror which collects the incoming light onto a single-pixel high-bandwidth InGaAs detector. The instrument has been designed to maximize detection efficiency and uniformity within a 20 mrad field of view. An external cryoradiator is thermally coupled to the receiver detector to cool the detector to -65 °C during science data passes over the lunar South

Pole. The detector temperature is cold-biased and stabilized by a heater. The APLE is tuned to maximize the signal-to-noise ratio (SNR) for the expected signal conditions. The APLE amplifies and reads the detector signal at 100 kHz, and the detector analog signal is then digitized by the DPLE.

.

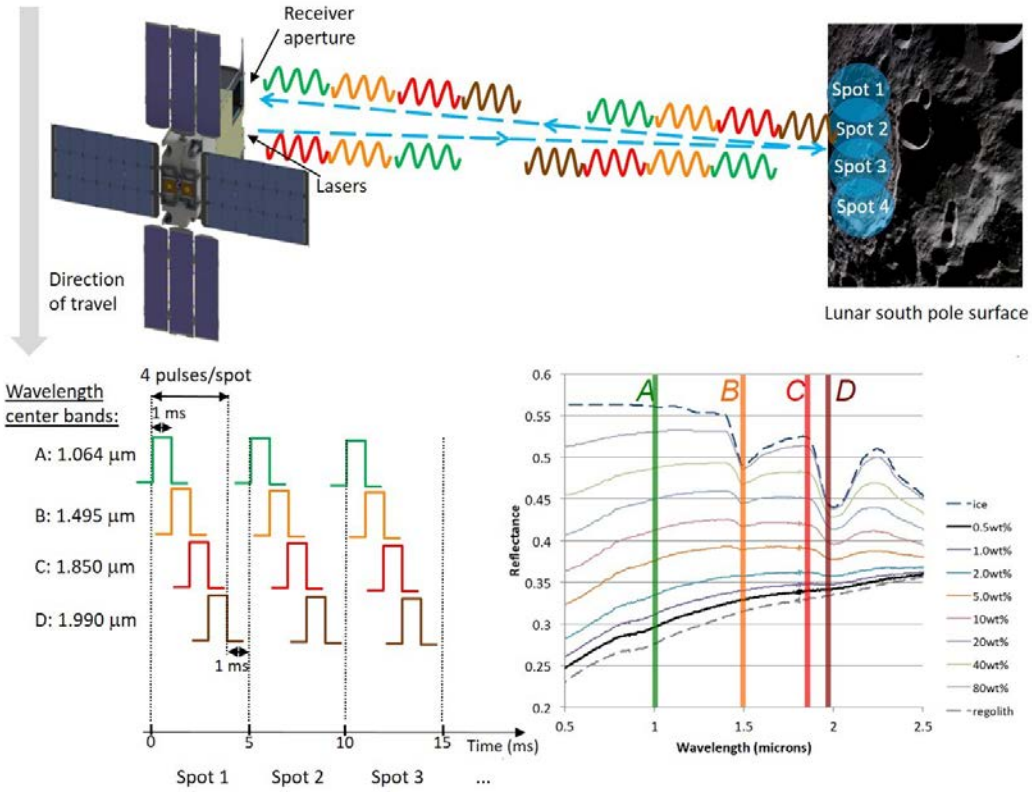

Figure 3-2 a) LF Operations concept indicating four sequentially pulsed bands of laser illumination and corresponding spots on the lunar surface. b) lower right: reflectance spectrum (bidirectional reflectance) for different water ice contents in lunar regolith.

In nominal operation, the LF lasers fire sequentially for 1-5 ms each, followed by a pause of 1-5 ms with all lasers off. The optical receiver collects and measures a portion of the light reflected from the lunar surface. The measurement with all lasers off quantifies the background, which is the sum of detector dark current, thermal emission from the receiver itself incident on the science detector, and solar illumination reflected from the lunar surface and detected by the instrument from both inside and outside its field of view (FOV). The instrument background is subtracted in post-processing from the measured signals. In order to increase the SNR, the measurements are averaged for each of the spectral band over the time in which the laser-illuminated FOV moves a distance on the lunar surface corresponding to the desired mapping resolution of lunar water ice (1-10 km).

As depicted in Figure 3-2b, two of the four wavelengths (~1495 nm and ~1990 nm) correspond to absorption peaks for water ice, while the two other wavelengths (~1064 nm and ~1850 nm) correspond to nearby continuum. Post processing algorithms will be used on the ground to derive the reflectance of the lunar surface at each of the four wavelengths. The continuum/absorption reflectance band ratios are then analyzed to quantify the weight percent of water ice (wt%) in the illuminated FOV. During the planned 2-month primary mission, LF will pulse the lasers for 2-3 minutes during ten near-

rectilinear orbits with periods of ~5 days, at altitudes of 13-53 km within 10° latitude of the lunar South Pole. The instrument operations concept is depicted in Figure 3-2a.

4. OPTICAL RECEIVER DESIGN

4.1 Optical design

The LF instrument optical receiver is a simple optical design using a 70 mm aperture rectangular off axis paraboloid (OAP) uncoated aluminum mirror. This optical system is housed in a 1U receiver housing which encompasses a baffle system optimized for this application by Photon Engineering LLC using the FRED non-sequential ray trace package. The detector is a 2 mm diameter extended-InGaAs photodiode with 2.4 micron cutoff supplied by Teledyne Judson Technologies, LLC. This design and baffling arrangement is shown in Figure 4-1. Table 1 indicates the principal technical specifications of the receiver design.

The goals of the optical design are to (1) maximize the detection efficiency of reflected laser photons, (2) minimize the stray light detection from outside the receiver FOV, and (3) match the FOV of the receiver to the divergence of the laser with margins to accommodate receiver-to-laser pointing instabilities. The optimization is done with respect to the point source transmittance function (PST), which conveniently treats the optical transfer function in angle space.

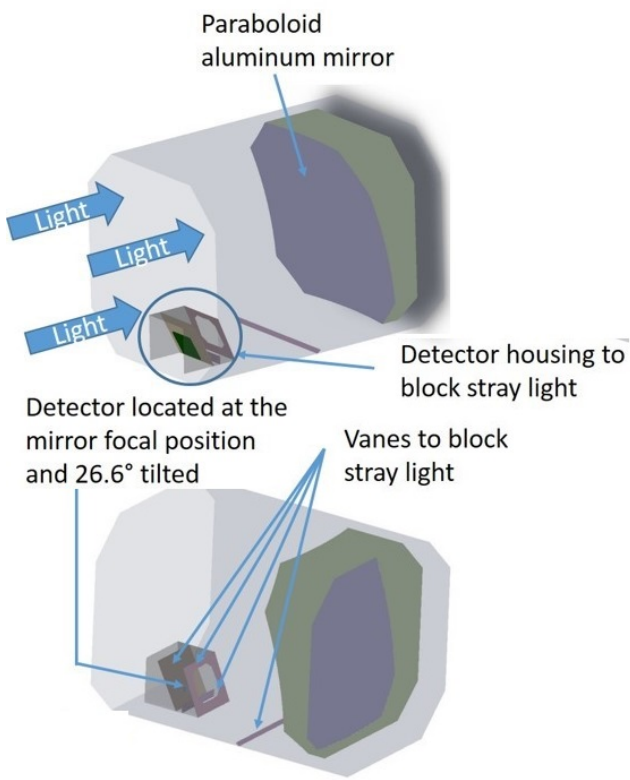

Figure 4-1 Optical design showing baffles.

Receiver dimensions	100×75×75 mm
Receiver aperture	75×75 mm
Mirror	• 70×70 mm bare aluminum off-axis paraboloid mirror, post-polish • Radius of curvature: 140 mm • Surface accuracy: 2λ @ 632.8 nm • RMS roughness: <30 Å
Detector	• 2.4 µm cutoff extended-InGaAs Teledyne Judson 2 mm diameter detector • Thermally isolated from the receiver structure and cooled to -65°C by a cryoradiator and thermally stabilized by a heater (the cryoradiator is not shown on Figure 4; see Figure 8)

Table 4-1 Technical specifications of the current receiver design.

In order to estimate the science performance of a given receiver optical design as a function of the predicted orbits and lunar surface illumination, our mission-level performance model uses the receiver point source transmittance (PST) function calculated in FRED[28] (see Figure 4-2 left). This is effectively the fraction of flux at the receiver aperture that

reaches the detector active area as a function of the θ_x and θ_Z incident field angles, where θ_x and θ_z are respectively the rotation angles around axes X and Z, the XZ plane being perpendicular to the receiver optical axis. The PST thus represents the receiver detection efficiency as a function of θ_x and θ_z. Different configurations were analyzed with the mission performance model to derive the optimized receiver optical design depicted in Figure 4-1. Figure 4-2b shows the predicted rotational average of the PST function (used in our mission-level performance model) corresponding to the final receiver design.

We note that the maximum value of the PST is equal to 0.68 (68% of the light at the receiver aperture reaches the detector active area), which is significantly less than 1. The primary reason for this is that the PST calculation is normalized to the flux passing through an unobscured 75 mm square entrance aperture, rather than the smaller and more complex mirror shape of the actual receiver. Additional power losses come from the mirror reflectivity modeled as 94.5% (reflectance of Al at a wavelength of 1 µm), the detector surface reflectivity modeled as 3%, and losses due to vignetting by the detector housing (which obstructs a part of the receiver aperture). Figure 4-2 right depicts the central portion of the 2D PST function for small θ_x and θ_Z incident angles to illustrate the receiver FOV. The color scale corresponds to the fraction of photons at the receiver aperture reaches the detector active area The black circle represents the 20 mrad receiver FOV.

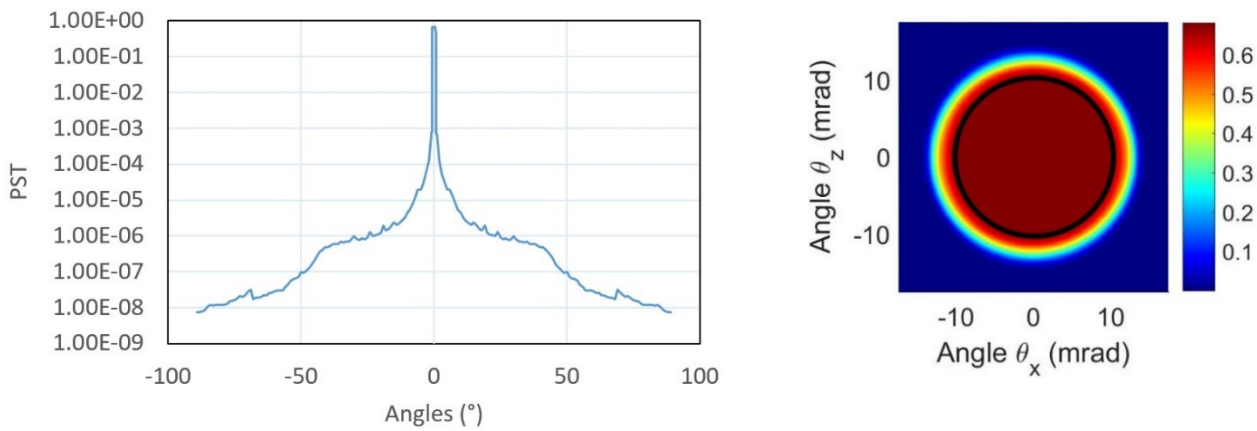

Figure 4-2 Rotationally averaged receiver point source transmittance (PST) function (left) and receiver FOV in angle space (right)..

4.2 Detector Performance.

The receiver's InGaAs detector sits at prime focus, bonded to a molybdenum alloy post to conduct heat to an adjacent titanium flexure-mounted cryoradiator. This post is epoxy bonded into a titanium alloy detector housing, which provides the necessary thermal isolation from the receiver housing. The detector housing uses a semi-kinematic 3-2-1 screw attachment to the receiver housing. The planes of the mating surfaces are oriented so that they provide athermal detector positioning, given the mixed materials in the assembly. The detector position relative to the mirror is set by machine tolerances at the mirror to receiver housing interface, and by shim thickness at the detector to housing interface. Dimensional inspection data for each of the components in the mechanical path between mirror and detector will be collected and reduced into shim values to achieve a nominal detector position.

The detector will be operated in flight at a nominal temperature of -65 °C to minimize dark current. At this temperature, the dark current is equal to ~1 nA. We selected a 2.4 µm wavelength cutoff to accommodate our longest laser wavelength of 1990 nm. Our thermal control system will keep the detector at 65 °C ± 1 °C during the observing phase of the mission.

5. LASER SUBSYSTEM

5.1 Diode lasers for flight

The key to fitting a four band IR laser reflectometer into a 2U package is the compact high power laser emitter assembly. The laser package, supplied by Coherent DILAS, Inc. uses diode lasers in a stacked arrangement with 19 emitters per bar. There are two bars per wavelength as indicated in Figure 5-1. These emitters project their beam into a custom two lens optical system called the BTS (beam transformation system) which results in an combined rectangular beam profile with divergence of less than 17.5 mrad (determined by 99.6% encircled energy). Due to varying efficiencies between the different wavelengths, supplying each laser with 45 A input current results in unequal optical output powers of 72 W, 30 W, 14 W, 14 W for the 1064 nm, 1495 nm, 1850 nm, and 1990 nm modules, respectively (please see Table 2).

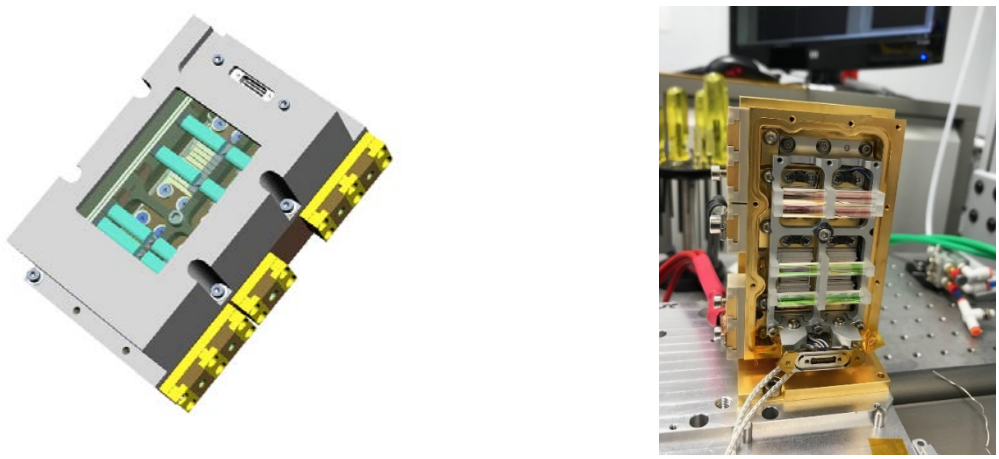

Figure 5-1 CAD view of laser package showing stacks of emitter and the 8 BTS assemblies (left). EM laser in test with cover removed showing BTS lens assemblies (right).

5.2 Laser requirement and FM testing

The FM laser assembly has gone through acceptance testing and meets the requirements (listed in Table 2). The FM laser has proved to provide a stable light-current-voltage (LIV) relationship (Figure 5-2 left), which is monotonic and linear with temperature variation, which will allow precise pre-launch calibration. For our FM laser, the measured far-field profile of the FM Laser (Figure 5-2 right) shall meet the 17 mrad divergence requirement and also the 1.3 mrad co-alignment (beam to beam) requirement after test. A qualification program provides confidence that the FM laser will operate within these specifications on orbit.

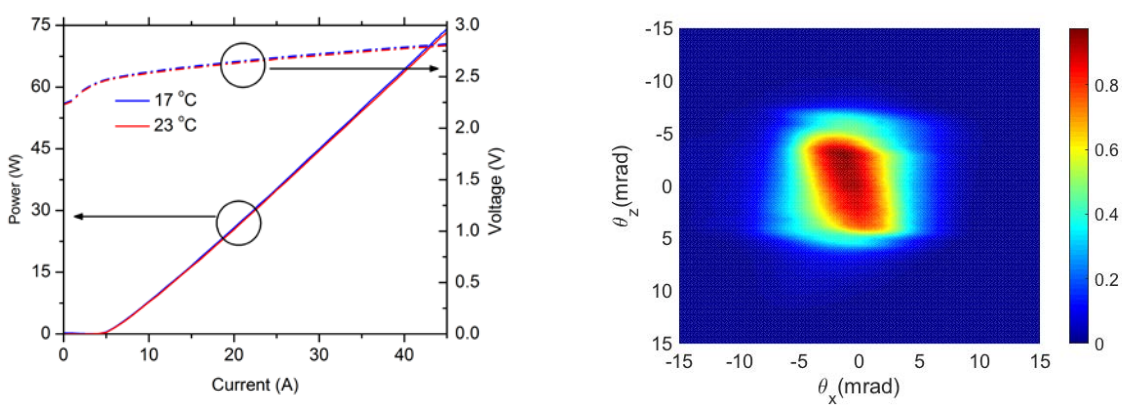

Figure 5-2 The LIV curve optical power and voltage relation to current (left) and the far field profile of FM laser (right).

	Topic	Specification	Value
Specifications	Wavelength Bands	Center Wavelength: Band A	1064 nm ±20 nm
		Center Wavelength: Band B	1495 nm ±20 nm
		Center Wavelength: Band C	1850 nm ±20 nm
		Center Wavelength: Band D	1990 nm ±20 nm
	Optical Power	Peak Output Power: Band A	≥35 W Peak
		Peak Output Power: Band B	≥25 W Peak
		Peak Output Power: Band C	≥14 W Peak
		Peak Output Power: Band D	≥14 W Peak
		Max Voltage per Stack at Rated Power	<2.8 V
		Current	<45 A
	Operating Mode: Each Band	Duty Cycle	20%
		Pulse Width	1 ms
		Frequency	200 Hz
	Beam Profile	Beam Delivery	Direct Beam
		Angular Content: All Bands	≤17 mrad Residual Divergence (99.6% Power
		Pointing Error: Band-to-band	<1.3 mrad
	Packaging	Cooling Method	Conductively Cooled
		Operating Temperature	17 °C – 23 °C
		Mass	≤750 g
		Envelope Dimensions	~9.6x6.2x4.18 cm^3
		Volume	≤250 cm^3

Table 5-1 Flight Requirements on DILAS laser package.

6. OPTOMECHANICAL DESIGN

6.1 Mechanical Design for Alignment

The opto-mechanical design of the LF instrument, depicted in Figure 6-1, comprises two subsystems: the laser and receiver modules, mounted to the sideplate and attached to an external radiator. The laser assembly is contained in an enclosure with copper heatsink, which is bolted to an aluminum alloy chassis containing phase-change material (PCM). This PCM chassis, in addition to its thermal function, also forms the mechanical foundation for the receiver module.

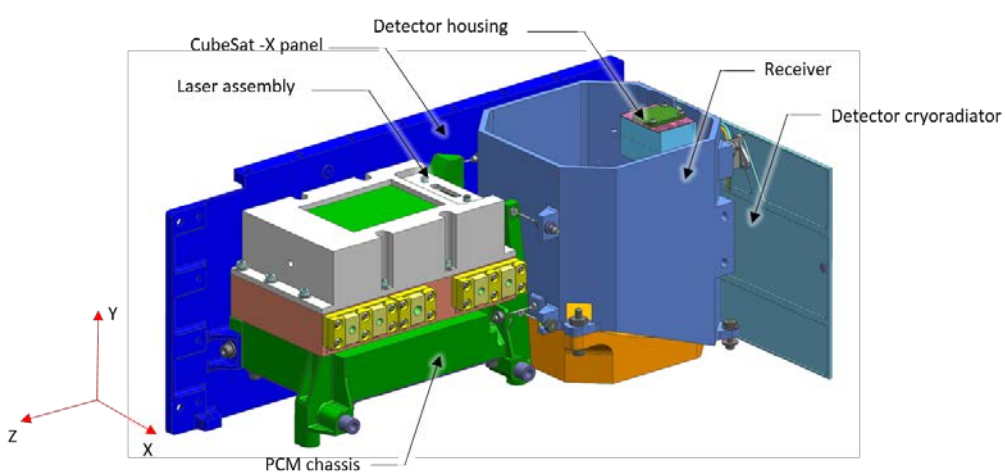

Figure 6-1 LF reflectometer optomechanical assembly. The assembled reflectometer optomechanical assembly is attached semi-kinematically through the rigid PCM chassis mounting features to the -X and -Y structural panels of the spacecraft.

The receiver module has an octagonal aperture, fastened to a machined aluminum housing. First-order athermalization is achieved through the shared use of aluminum alloy 6061-T6 between the post-polished, diamond-turned, off-axis paraboloidal mirror and the receiver housing. The mirror's mounting pads are diamond-turned to their final profile in the same lathe operation as used to machine the optical surface, providing a high degree of precision in the pad co-planarity/parallelism. The pads that interface the mirror to the receiver housings are similarly diamond turned in one lathe operation. Mirror-to-receiver-housing location is maintained through a close slip-fit sleeve with a concentric fastener. This alignment feature is coincident with the mirror optical axis and functions as the primary tooling feature for turning operations. A secondary slotted hole on one of the other mounting pads uses a similar sleeved fastener to control clocking of the mirror. The combination of these features allows an adjustment-free "snap together" integration approach.

6.2 Precision alignment of laser and receiver

The mechanical connection between the receiver and laser modules is achieved via six titanium-alloy rod flexures (see Figure 6-2). These "stingers" provide compliant attachment as well as thermal isolation between the laser and receiver while maintaining boresight alignment. Limited relative pointing adjustment is achieved by differential shimming between seats machined into the receiver housing, the PCM chassis, and the stingers.

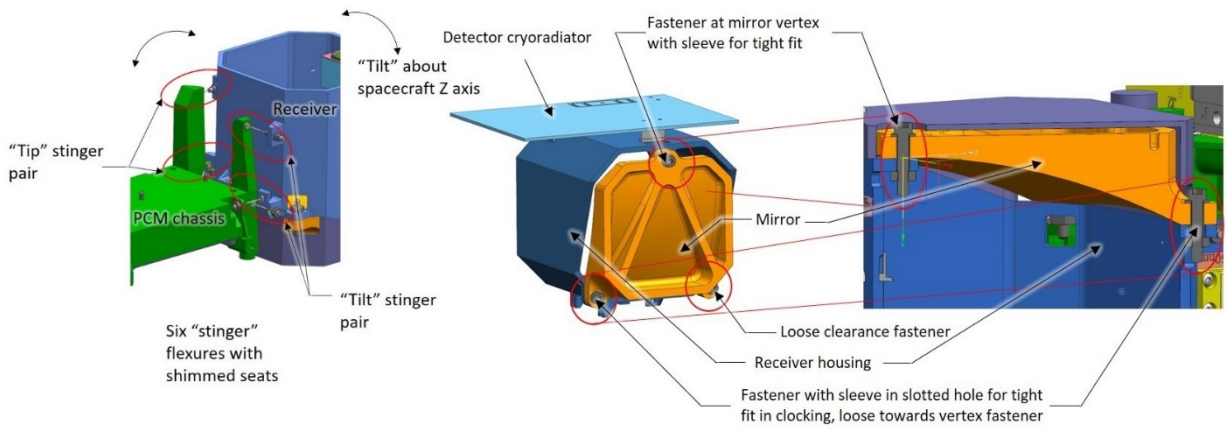

Figure 6-2 Receiver module to PCM chassis connection showing six stinger flexures with pairs oriented for tip-tilt shim adjustment relative to laser module boresight (left) and section view (right) showing fastener detail of semi-kinematic snap-together design. The external surfaces of the receiver housing are electro-plated with gold to provide passive cooling.

7. PAYLOAD ELECTRONICS

7.1 Single string COTS electronics

The compact volume and power constraints of the LF CubeSat made it a challenge to develop electronics for this instrument. The payload electronics comprise two boards (PWA's), the payload digital board,(DPLE) which controls the instrument and manages command and telemetry, and analog board (APLE) which carries the AD converters for the science detector and the housekeeping (thermal, current and voltage) sensors. The architecture of the payload electronics is shown in Figure 7-1 (left), which shows the connections between these boards and the L_EPS boards. The actual flight DPLE and L_EPS boards are also shown in Figure 7-1 (right). The risk philosophy of the CubeSat project allowed use of COTS components where prudent, but required detailed inventory of all electronics components to determine tolerable radiation levels (SEL, TID) to prevent destructive latch-up and ensure reliable performance in harsh environments.

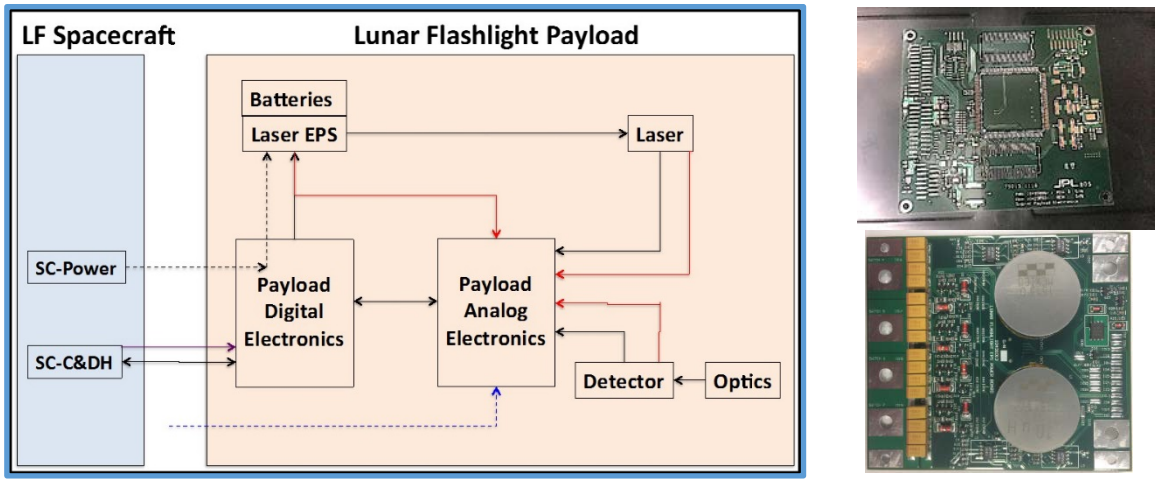

Figure 7-1 Payload electronics boards and connections (left), DPLE flight board (upper right), and L_EPS flight board (lower right).

The architecture of the electronics provides a single point of connection from the DPLE to the spacecraft electronics via a single 25 pin connector which carries spacecraft power and LVDS Spacewire for communication. The DPLE board manages the APLE board to control acquisition of data from the detector as well as housekeeping data. The data for a science pass is stored in local SDRAM (2Gbit) until the end of the laser activity, and then is retrieved by the spacecraft computer over Spacewire and downlinked to ground. Actel FPGA's on the DPLE and APLE control the laser sequencing and the data acquisition. Thermal control and fault protection logic is implemented on the spacecraft CPU. The front end electronics on the APLE will be tuned during instrument calibration to optimize signal to noise (SNR) performance, based on LF mission objectives and specific laser firing sequence.

7.2 Laser power system.

The Laser power electronics (L_EPS) board (Figure 7-1c) provides power to the laser assembly via four FET switches, and draws current from the dedicated payload battery. The payload battery comprises three Li-ion cells designed to supply 16 Whr total of laser power at end of life (EOL), and which have gone through a rigorous screening program. Destructive testing was performed on these cells and the lessons learned were incorporated into the flight packaging design. The L_EPS system is able to deliver 45A of current to each laser during the firing sequence. The operating temperature of the batteries is managed by a dedicated thermal control system controlled by the spacecraft flight software. There are also challenges to managing the thermal environment of the L_EPS boards since the power board generates up to 59 W of thermal load which needs to be dissipated by the spacecraft bus during the laser firing sequence. This is accomplished via optimized copper thermal straps connected to the CubeSat frame. The electronics are guarded against over-current over-temperature conditions by sensors and fault protection logic which will shut down the laser if the electronics or the laser overheat.

8. THERMAL DESIGN

Perhaps the greatest challenge in the design of a 2U active laser reflectometer is the management of heat dissipated by the high power (70 W) diode laser and the associated power electronics. The laser is mounted on an aluminum box containing phase change material (PCM) supplied by KULR Technologies, Inc. (see Figure 8-1 left), which will act as a heat sink for the duration of the laser firing sequence, which will nominally last 2-3 minutes during an encounter with the lunar South Pole. The nominal laser firing temperature is 20 °C and will be held to under 25 °C for this duration, as the PCM material (paraffin) melts. After the encounter, the thermal energy is dissipated into the spacecraft structure and radiated away from the CubeSat during the remainder of the (5-7 day) orbit. It can be seen in Figure 8-1 b, that the radiator stays cold (blue) and is adjacent to a hot (red) L_EPS module.

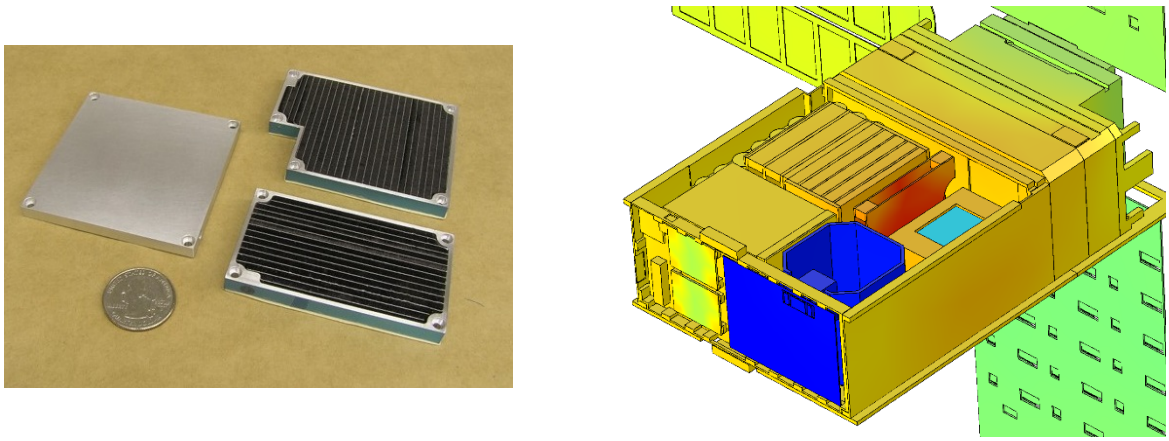

Figure 8-1 Phase Change material (left) and thermal profile of LF CubeSat showing cold receiver and radiator in blue and hot L_EPS in red.

As mentioned, the other thermal challenge is to dissipate the heat from the L_EPS power electronics which is accomplished by custom copper heat straps. Finally, the detector temperature is managed by a dedicated radiator which is mounted to the receiver housing and connected to the molybdenum cold finger that holds the detector. The detector temperature is stabilized by a cold biased thermal control system and a thermal sensor (Lakeshore DT-670) also mounted on the cold finger as shown in Figure 9, with a heater mounted on the radiator near the detector assembly. The exterior of the receiver housing is gold plated to reduce thermal loading on the receiver.

In summary, the thermal environment of the LF instrument is managed by three active thermal loops: (1) the cold biased detector is held at -65 °C during data acquisition, (2) the laser and PCM material is held at 20 °C in preparation for laser activation, and (3) payload battery temperature is maintained at approximately 10 °C, dictated by compatibility with laser operation.

9. INSTRUMENT SYSTEM ENGINEERING

9.1 Instrument Noise Budget

The key challenge in the design of the LF instrument was to guarantee a return of science data with high enough signal to noise ratio (SNR) to render statistically meaningful scientific measurements. Although each subsystem has been designed to minimize the noise, the SNR related to the measured reflectance for each individual return pulse does not meet this threshold. As in many optical scanning instruments, the LF detector readings must be integrated along track for an interval consistent with the a priori characterization of the target to reduce the uncertainty due to instrument noise. Hence, the key is to average the measurements for a given mapping resolution to increase the SNR, assuming the ice content and reflectance are homogeneous within the corresponding (10 km) lunar ground track.

We have developed a model that computes the estimated SNR as a function of the spacecraft position based on predicted orbital trajectories of the LF spacecraft. The main noise contributions that our model takes into account are shown in Table 9-1. The shot noise contribution related to the detected solar background was computed using the receiver angular detection efficiency, complex lunar topography at a resolution of 475 m/pixel[30], three-dimensional solar and earthshine illumination of the moon (using the illumination model from Paige et al.[3]), and planned orbital trajectories of the LF spacecraft. We can clearly see here above that the main noise source comes from the detector electronics. Let us note that the dark current should be null for a perfectly unbiased detector, but there is always a residual bias generating some dark current; we have considered a dark of 1nA in our case based on some preliminary measurements using the detector in flight environmental conditions. The detector current related to the detected lasers photons varies between 10 pA and 329 pA, depending on the altitudes and the wavelength, whereas the maximum detector current due to the detected thermal emission from the instrument is equal to 137 pA @ 264K assuming the emission of a black body (very conservative case).

Primary Sources of Instrument Noise
• detector Johnson-Nyquist thermal noise: 76 fA/$\sqrt{Hz}$
• detector dark current shot noise: 18 fA/$\sqrt{Hz}$
• detected laser photons shot noise: 1.8 – 10.3 fA/$\sqrt{Hz}$, depending on the altitudes and the wavelength
• detector electronics noise: 0.5 pA/$\sqrt{Hz}$
• shot noise from instrument thermal emission incident on the detector: max.6.6 fA/$\sqrt{Hz}$ at a mirror temperature of 264K
• shot noise related to the detected solar background: 0.071 - 47.3 fA/$\sqrt{Hz}$ depending on the spacecraft position
• Instability of the laser EPS: σ=0.075% considering an integration time of 6 ms.

Table 9-1 Primary sources of Lunar Flashlight instrument noise

Figure 9-1 depicts the SNR on the reflectance measurements as a function of the operational time for each band and for a lunar mapping resolution of 10 km. The regions where the SNR drops to zero indicate very bright spots on the Moon surface that saturate the detector electronics. For the regions where SNR>0, SNR variations as a function of time are mainly due to altitude changes.

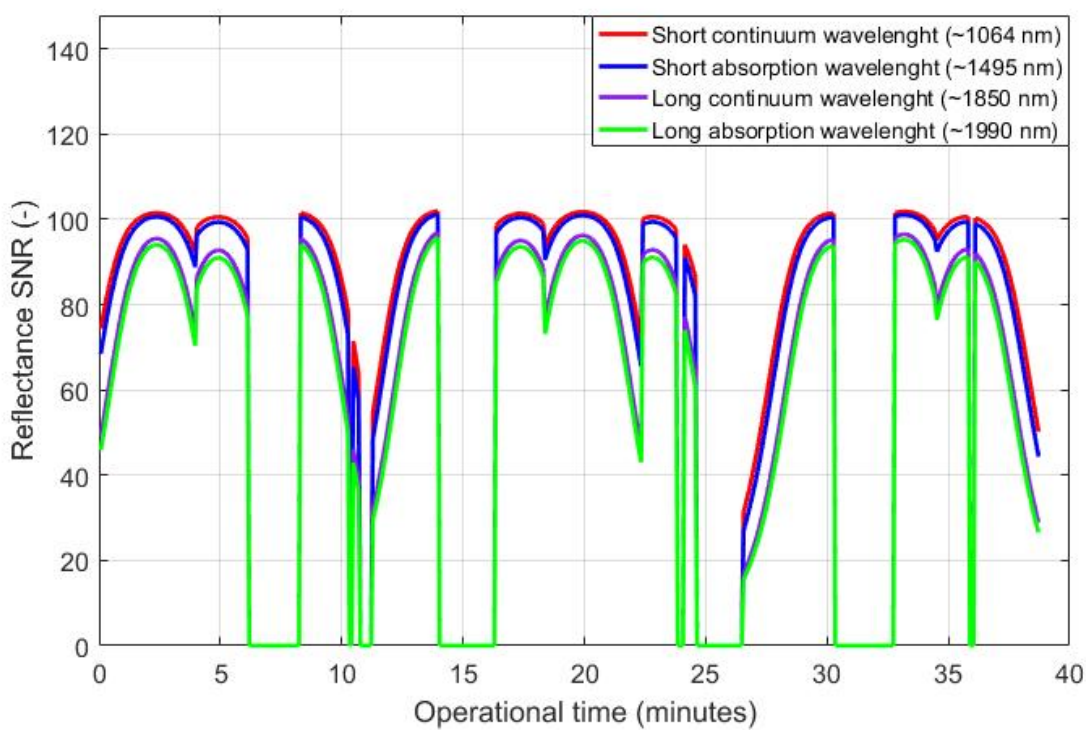

Figure 9-1 Estimated reflectance SNR for a lunar mapping resolution of 10 km.

We are currently developing techniques to implement a ground testbed which would enable end-to-end radiometric relative calibration of the LF instrument. The goal will be to achieve radiometric calibration accuracy better than 0.5% relative to the adjacent operational bands. It should be noted, however, that an on-orbit calibration might also be achieved by targeting dry spots on the Lunar surface. In addition, as mentioned previously, the 1.064 µm band has been chosen to enable comparison with data acquired by the Lunar Orbiter Laser Altimeter (LOLA), which had been radiometrically calibrated. Thus it shall be possibile to also to perform a retro-calibration of LF based on the comparison of measurements acquired by LOLA on the same spots on the Lunar surface.

9.2 Thermal and Power budgets

In addition to the noise budget, the instrument system engineering requires management of the thermal and power resouces, both of which determine the duration for which it is possible to safely operate the laser. Ultimately, it is the volume of the PCM material which determines the length of time to operate the laser before exceeding safe temperatures limits. The thermal straps on the L_EPS electronics, however have been sized to the maximum that can be accommodated in the constrained volume. These will allow up to 2-3 minutes of laser operation. Surprisingly, the payload Li-ion batteries are not the limiting factor in the laser runtime, consequently the number of cells (3) has been chosen to match the maximum laser run time set by thermal constraints.

9.3 Engineering Trades

Several key design trades were conducted as instrument systems competed for volume and other resources. Firstly, the size of the receiver OAP was a significant trade since it determined the number of photons available to the detector. Thanks to a compact laser emitter, this trade was a good balance where we could allocate almost 1U to the receiver and provide a 70 cm entrance pupil. Similarly, our electronics, particularly on the APLE board, which contains the ADC for the detector, was limited in the complexity of the electronics which could be fit on board. Given more volume, we would anticipate a more sophisticated low noise design for our front end electronics. Thirdly, as already mentioned, the thermal design drove the overall system engineering in that the size of the thermal straps to the L_EPS electronics, and the unavailability of a second radiator to cool the laser subsystem forced us to limit laser operation to 2-3 minutes per pass.

9.4 Data management

As mentioned, the LF instrument stores the complete data set for a pass in its onboard SDRAM (2 Gbit) for later transfer to the spacecraft over the Spacewire to a flash RAM buffer, and then downlink to ground. Due to limits on data storage resources on board, we expect to downlink the data from each pass during ground passes prior to the next encounter. Considering the low TRL of our laser system and the demands on accurate knowledge of the optical power for each laser emitter during the science pass, we downlink all associated housekeeping telemetry, such as laser temperature, current, voltages, as well as battery parameters and detector temperature to aid in the post processing on ground. For this reason, we have configurable telemetry tables which enable the downlink of tailored diagnostic and housekeeping data. Naturally the volume of housekeeping telemetry may come at the expense of experiment duration, as a compact science data set will allow more margin in the onboard data storage, especially in the case of missed downlink opportunities.

9.5 Instrument Model Philosophy

As LF is a CubeSat, we have followed a “proto-flight” (PF) model philosophy for the instrument in that environmental and functional tests are performed on the “flight model” (FM) hardware, although possibly at reduced levels. For the LF payload, we have maintained a hybrid approach where critical low-TRL hardware, such as the laser, follow a traditional EM/FM philosophy. Hence, we have tested an “engineering model” (EM) laser and found an issue which aided the vendor in construction of the FM, particularly to maintain a more compact beam to meet beam co-alignment requirements. Furthermore, our EM laser underwent multiple vibration tests to determine structural susceptibility to vibration. While our optics and receiver are proto-flight, we have performed tests on detector flight spares and practiced assembly techniques on non-flight hardware to reduce risk. For the somewhat novel (although not low-TRL) PCM thermal hardware, we have a spare to guard against any anomalies (such as leakage) in the flight model during test. All electronics are proto-flight and developed without an EM, although there was a “breadboard” for the L_EPS electronics.

10. MISSION OPERATIONS AND SCIENCE DATA PROCESSING

10.1 Mapping vs detection

The baseline LF mission will consist of 11 orbits with 10 science passes over the lunar South Pole. For each pass, there will be 2 to 3 minutes of laser activation time which will be directed at selected PSRs based on our knowledge of the lunar landscape and prior simulations. The LF instrument allows us to change the pulse duration (nominally 1 msec), as well as the laser sequence. This will allow flexibility in case of a laser anomaly, or in case of unexpected levels of stray light fluctuation. In addition, the instrument will support execution of multiple laser sequences per orbit, enabling us to target specific PSRs, and allowing us to conserve laser power and thermal run time when over non-PSR features.

Since the raw detector data is downlinked to ground, the along-track distance over which to integrate an estimate of the water content remains a parameter which can be changed during the post processing. Similarly, the downlink of complete housekeeping data will enable effective noise suppression algorithms during ground analysis. All data is tagged with a unique timestamp that will be correlated to spacecraft position and pointing data provided by the attitude control system.

10.2 Calibration on ground and on orbit

A key to recovering high SNR data from the flight data set is to use the housekeeping data in the context of the spacecraft and instrument thermal and electrical environment. For this reason, we intend to do extensive calibration of both the laser and the detector under the thermal range and electrical (current and voltage) ranges expected during on orbit operation. In particular, extensive work has gone into the calibration of the laser output optical power based on the onboard temperature, current and voltage during each pulse. Housekeeping data will be available at up to 100 kHz to provide modeling data to determine the power delivered by each 1msec laser pulse. Similarly, the detector data will have the same time resolution.

Further ground post processing and analysis of the reflectance data obtained in flight will also be correlated with past data sets taken at 1064 nm with the LOLA instrument on the LRO mission.

11. CONCLUSION

We have presented the top level design of the Lunar Flashlight Instrument and described the key subsystems and novel technologies involved in designing a CubeSat form factor active SWIR reflectometer. We have also presented some of the system engineering challenges encountered in this design effort.

The Lunar Flashlight CubeSat is currently undergoing integration and test with a delivery date in late 2018. The LF instrument has undergone opto-mechanical I&T and initial functional testing of the flight hardware. It is anticipated that extensive time will be spent on calibration, where we have been developing techniques to perform a relative spectral calibration of our ground support equipment that will enable precise laser power output determination of all four laser spectral bands.

We expect that the EM-1 SLS mission will be launched no sooner than December 2019 with a deployment of the Lunar Flashlight CubeSat to the first “bus stop” on its CIS-lunar journey. In the course of locating and quantifying lunar water ice, this mission will demonstrate several novel and key technologies to enable CubeSat science return.

ACKNOWLEDGEMENT

The Lunar Flashlight mission is funded by the Advanced Exploration Systems program in the Human Exploration and Operations (HEO) mission directorate of the National Aeronautics and Space Administration (NASA). We acknowledge the contributions of our partners Coherent DILAS Diode Laser, Inc, Sierra Lobo, Inc., Photon Engineering, LLC, and KULR Technology, Inc. Part of this work was performed at the Jet Propulsion Laboratory, California Institute of Technology, under contract with NASA.

REFERENCES

[1] Goddard, R. H., [The Papers of Robert H. Goddard: 1898-1924], McGraw-Hill, New York, 413-430 (1970).

[2] Watson, K., Murray, B. and Brown, H., "On the possible presence of ice on the Moon," Journal of Geophysical Research 66(5), 1598-1600 (1961).

[3] Paige, D. A., Siegler, M. A., Zhang, J. A., Hayne, P. O., Foote, E. J., Bennett, K. A., Vasavada, A. R., Greenhagen, B. T., Schofield, J. T., McCleese, D. J., Foote, M. J., DeJong, E., Bills, B. G., Hartford, W., Murray, B. C., Allen, C. C., Snook, K., Soderblom, L. A., Calcutt, S., Taylor, F. W., Bowles, N. E., Bandfield, J. L., Elphic, R., Ghent, R., Glotch, T. D., Wyatt, M. B. and Lucey P. G., "Diviner lunar radiometer observations of cold traps in the Moon's south polar region," Science 330(6003), 479-482 (2010).

[4] Hayne, P. O., Hendrix, A., Sefton-Nash, E., Siegler, M. A., Lucey, P. G., Retherford, K. D., Williams, J. P., Greenhagen, B. T. and Paige, D. A., "Evidence for exposed water ice in the Moon's south polar regions from Lunar Reconnaissance Orbiter ultraviolet albedo and temperature measurements," Icarus 255, 58-69 (2015).

[5] Hayne, P. O., Paige, D. A., Ingersoll, A. P., Judd, M. A., Aharonson, O., Alkali, L., Byrne, S., Cohen, B., Colaprete, A., Combe, J. P. and Edwards, C., "New Approaches to Lunar Ice Detection and Mapping: Study Overview and Results of the First Workshop," Report of the Annual Meeting of the Lunar Exploration Analysis Group 1748, 7043 (2013).

[6] The Lunar Exploration Analysis Group (LEAG), the Mars Exploration Program Analysis Group (MEPAG) and the Small Bodies Assessment Group (SBAG), "Strategic Knowledge Gaps (SKGs)," NASA, 29 August 2016, < https://www.nasa.gov/exploration/library/skg.html > (19 September 2016).

[7] Thomson, B. J., Bussey, D. B. J., Neish, C. D., Cahill, J. T. S., Heggy, E., Kirk, R. L., Patterson, G. W., Raney, R. K., Spudis, P. D., Thompson, T. W. and Ustinov, E. A., "An upper limit for ice in Shackleton crater as revealed by LRO Mini-RF orbital radar," Geophysical Research Letters 39(14) (2012).

[8] Spudis, P. D., Bussey, D. B. J., Baloga, S. M., Cahill, J. T. S., Glaze, L. S., Patterson, G. W., Raney, R. K., Thompson, T. W., Thomson, B. J. and Ustinov, E. A., "Evidence for water ice on the Moon: Results for anomalous polar craters from the LRO Mini-RF imaging radar," Journal of Geophysical Research: Planets 118(10), 2016 -2029 (2013).

[9] Nozette, S., Lichtenberg, C. L., Spudis, P., Bonner, R., Ort, W., Malaret, E., Robinson, M. and Shoemaker, E. M., "The Clementine bistatic radar experiment," Science 274(5292), 1495-1498 (2016).

[10] Feldman, W. C., Maurice, S., Binder, A. B., Barraclough, B. L., Elphic, R. C. and Lawrence, D. J., "Fluxes of fast and epithermal neutrons from Lunar Prospector: Evidence for water ice at the lunar poles," Science 281(5382), 1496-1500 (1998).

[11] Feldman, W. C., Lawrence, D. J., Elphic, R. C., Barraclough, B. L., Maurice, S., Genetay, I. and Binder, A. B., "Polar hydrogen deposits on the Moon," Journal of Geophysical Research 105(E2), 4175-4195 (2000).

[12] Feldman, W. C., Lawrence, D. J., Little, R. C., Lawson, S. L., Gasnault, O., Wiens, R. C., Barraclough, B. L., Elphic, R. C., Prettyman, T. H. and Steinberg, J. T., "Evidence for water ice near the lunar poles," Journal of Geophysical Research, 106(E10), 23231-23251 (2001).

[13] Mitrofanov, I. G., Sanin, A. B., Boynton, W. V., Chin, G., Garvin, J. B., Golovin, D., Evans, L. G., Harshman, K., Kozyrev, A. S., Litvak, M. L. and Malakhov, A., "Hydrogen mapping of the lunar south pole using the LRO neutron detector experiment LEND," Science 330(6003), 483-486 (2010).

[14] Mitrofanov, I., Litvak, M., Sanin, A., Malakhov, A., Golovin, D., Boynton, W., Droege, G., Chin, G., Evans, L., Harshman, K. and Fedosov, F., "Testing polar spots of water-rich permafrost on the Moon: LEND observations onboard LRO," Journal of Geophysical Research: Planets 117(E12) (2012).

[15] Boynton, W. V., Droege, G. F., Mitrofanov, I. G., McClanahan, T. P., Sanin, A. B., Litvak, M. L., Schaffner, M., Chin, G., Evans, L. G., Garvin, J. B. and Harshman, K., "High spatial resolution studies of epithermal neutron emission from the lunar poles: Constraints on hydrogen mobility," Journal of Geophysical Research: Planets 117(E12) (2012).

[16] Livengood, T. A., Chin, G., Sagdeev, R. Z., Mitrofanov, I. G., Boynton, W. V., Evans, L. G., Litvak, M. L., McClanahan, T. P., Sanin, A. B. and Starr, R. D., "Evidence for Diurnally Varying Hydration at the Moon's Equator from the Lunar Exploration Neutron Detector (LEND)," Proc. Lunar and Planetary Science Conference 45, 1507 (2014).

[17] Schwadron, N. A., Wilson, J. K., Looper, M. D., Jordan, A. P., Spence, H. E., Blake, J. B., Case, A. W., Iwata, Y., Kasper, J. C., Farrell, W. M. and Lawrence, D. J., "Signatures of volatiles in the lunar proton albedo," Icarus 273, 25-35 (2016).

[18] Gladstone, G. R., Retherford, K. D., Egan, A. F., Kaufmann, D. E., Miles, P. F., Parker, J. W., Horvath, D., Rojas, P. M., Versteeg, M. H., Davis, M. W. and Greathouse, T. K., "Far-ultraviolet reflectance properties of the Moon's permanently shadowed regions," Journal of Geophysical Research: Planets 117(E12) (2012).
[19] Hendrix, A. R., Retherford, K. D., Randall Gladstone, G., Hurley, D. M., Feldman, P. D., Egan, A. F., Kaufmann, D. E., Miles, P. F., Parker, J. W., Horvath, D. and Rojas, P. M., "The lunar far-UV albedo: Indicator of hydration and weathering," Journal of Geophysical Research: Planets 117(E12) (2012).
[20] Colaprete, A., Schultz, P., Heldmann, J., Wooden, D., Shirley, M., Ennico, K., Hermalyn, B., Marshall, W., Ricco, A., Elphic, R. C. and Goldstein, D., "Detection of water in the LCROSS ejecta plume," Science 330(6003), 463-468 (2012).
[21] Heldmann, J. L., Lamb, J., Asturias, D., Colaprete, A., Goldstein, D. B., Trafton, L. M. and Varghese, P. L., "Evolution of the dust and water ice plume components as observed by the LCROSS visible camera and UV–visible spectrometer," Icarus 254, 262-275 (2015).
[22] Pieters, C. M., Goswami, J. N., Clark, R. N., Annadurai, M., Boardman, J., Buratti, B., Combe, J. P., Dyar, M. D., Green, R., Head, J. W. and Hibbitts, C., "Character and spatial distribution of OH/H2O on the surface of the Moon seen by M3 on Chandrayaan-1," Science 326(5952), 568-572 (2009).
[23] Sunshine, J. M., Farnham, T. L., Feaga, L. M., Groussin, O., Merlin, F., Milliken, R. E. and A'Hearn, M. F., "Temporal and spatial variability of lunar hydration as observed by the Deep Impact spacecraft," Science 326(5952), 565-568 (2009).
[24] Clark, R. N., "Detection of adsorbed water and hydroxyl on the Moon," Science 326(5952), 562-564 (2009).
[25] Zuber, M. T., Head, J. W., Smith, D. E., Neumann, G. A., Mazarico, E., Torrence, M. H., Aharonson, O., Tye, A. R., Fassett, C. I., Rosenburg, M. A. and Melosh, H. J., "Constraints on the volatile distribution within Shackleton crater at the lunar south pole," Nature 486(7403), 378-381 (2012).
[26] Lucey, P. G., Neumann, G. A., Paige, D. A., Riner, M. A., Mazarico, E. M., Smith, D. E., Zuber, M. T., Siegler, M., Hayne, P. O., Bussey, D. B. J., Cahill, J. T. S., McGovern, A., Isaacson, P., Corley, L. M., Torrence, M. H., Melosh, H. J., Head, J. W. and Song, E., "Evidence for Water Ice and Temperature Dependent Space Weathering at the Lunar Poles from Lola and diviners," Proc. Lunar and Planetary Science Conference 45, 2325 (2014).
[27] Fisher, E. A., Lucey, P. G., Lemelin, M., Greenhagen, B. T., Siegler, M. A., Mazarico, E., Aharonson, O., Williams, J. P., Hayne, P. O., Neumann, G. A. and Paige, D. A., "Evidence for surface water ice in the lunar polar regions using reflectance measurements from the Lunar Orbiter Laser Altimeter and temperature measurements from the Diviner Lunar Radiometer Experiment," Icarus 292, 74-85 (2017).
[28] Cohen, B. A., Hayne, P. O., Greenhagen, B. T., Paige, D. A., Camacho, J. M., Crabtree, K., Paine, C. G. and Sellar, R. G., "Payload Design for the Lunar Flashlight Mission," Proc. Lunar and Planetary Science Conference 48, 1709 (2017).
[29] Vinckier, Q., Hayne, P. O., Martinez-Camacho, J.M., Paine, C., Cohen, B. A., Wehmeier, U. J., and Sellar, R. G., "System Performance Modeling of the Lunar Flashlight CubeSat Instrument", Proc. Lunar and Planetary Science Conference 49, 1030 (2018).
[30] Smith, D. E., Zuber, M. T., Neumann, G. A., Lemoine, F. G., Mazarico, E., Torrence, M. H., McGarry, J. F., Rowlands, D. D., Head, J. W., Duxbury, T. H. and Aharonson, O., "Initial observations from the lunar orbiter laser altimeter (LOLA)," Geophysical Research Letters 37(18) (2010).
[31] Riris, H., Cavanaugh, J., Sun, X., Liiva, P., Rodriguez, M. and Neuman, G., "The lunar orbiter laser altimeter (LOLA) on NASA's lunar reconnaissance orbiter (LRO) mission," Proc. International Conference on Space Optics 8 (2010).
[32] Ramos-Izquierdo, L., Scott III, V. S., Connelly, J., Schmidt, S., Mamakos, W., Guzek, J., Peters, C., Liiva, P., Rodriguez, M., Cavanaugh, J. and Riris, H., "Optical system design and integration of the Lunar Orbiter Laser Altimeter," Applied Optics 48(16), 3035-3049 (2009).
[33] Clark, P. E., Malphrus, B., Brown, K., Hurford, T., Brambora, C., MacDowall, R., Folta, D., Tsay, M., Brandon, C. and Team, L. I. C., "Lunar Ice Cube: Searching for Lunar Volatiles with a lunar cubesat orbiter," Proc. AAS/Division for Planetary Sciences Meeting 48, 223.03 (2016).
[34] Hardgrove, C., Bell, J., Thangavelautham, J., Klesh, A., Starr, R., Colaprete, T., Robinson, M., Drake, D., Johnson, E., Christian, J. and Genova, A., "The Lunar Polar Hydrogen Mapper (LunaH-Map) mission: Mapping hydrogen distributions in permanently shadowed regions of the Moon's south pole," Proc. Annual Meeting of the Lunar Exploration Analysis Group 1863, 2035 (2015).
[35] Fisher, E. A., Lucey, P. G., Lemelin, M., Greenhagen, B. T., Siegler, M. A., Mazarico, E., ... & Paige, D. A. (2017). Evidence for surface water ice in the lunar polar regions using reflectance measurements from the Lunar Orbiter Laser Altimeter and temperature measurements from the Diviner Lunar Radiometer Experiment. *Icarus*, *292*, 74-85.